Giant Piezomagnetism in Mn_3NiN

David Boldrin[1‡], Andrei P. Mihai[2‡], Bin Zou[2‡], Jan Zemen[1,3], Ryan Thompson[1], Ecaterina Ware[2], Bogdan V. Neamtu[4], Luis Ghivelder[5], Bryan Esser[6], David W. McComb[6], Peter Petrov[2] and Lesley F. Cohen[1]*

1. Department of Physics, Blackett Laboratory, Imperial College London, London SW7 2AZ, United Kingdom

2. Department of Materials, Imperial College London, London SW7 2BP, United Kingdom

3. Faculty of Electrical Engineering, Czech Technical University in Prague, Technická 2, Prague 166 27, Czech Republic

4. Material Science and Technology Department, Technical University of Cluj-Napoca, 103-105 Muncii, Romania

5. Instituto de Fisica, Universidade Federal do Rio de Janeiro, 21941-972 Rio de Janeiro, RJ, Brazil

6. Center for Electron Microscopy and Analysis, 1305 Kinnear Road, Columbus, OH 43212, United States of America

KEYWORDS piezomagnetism, antiperovskite, non-volatile memory, antiferromagnet, spintronics

Abstract

Controlling magnetism with electric field directly or through strain-driven piezoelectric coupling remains a key goal of spintronics. Here we demonstrate that giant piezomagnetism, a linear magneto-mechanic coupling effect, is manifest in antiperovskite Mn_3NiN, facilitated by its geometrically frustrated antiferromagnetism opening the possibility of new memory device concepts. Films of Mn_3NiN with intrinsic biaxial strains of ±0.25% result in Néel transition shifts

up to 60K and magnetisation changes consistent with theory. Films grown on $BaTiO_3$ display a striking magnetisation jump in response to uniaxial strain from the intrinsic $BaTiO_3$ structural transition, with an inferred 44% strain coupling efficiency and a magnetoelectric coefficient α (where $\alpha = \frac{dB}{dE}$) of 0.018 G cm/V. The latter agrees with the 1000-fold increase over Cr_2O_3 predicted by theory. Overall our observations pave the way for further research into the broader family of Mn-based antiperovskites where yet larger piezomagnetic effects are predicted to occur at room temperature.

Introduction

A growing demand for improved non-volatile random access memory (RAM) motivates the exploration of many different forms of magnetoelectric (ME) control of magnetisation[1]. Technologies have evolved from monolithic ME effect in multiferroics, where direct control over antiferromagnetic (AFM) order has been achieved[2], to the development of artificial multiferroics[3], where the ME effect emerges from the coupling between layers with different functionality, for example ferroelectricity (piezoelectricity) and ferromagnetism (FM). The latter has enabled electrical tunability of magnetic transition temperatures[4], magnetic anisotropy[5,6], magnetisation amplitude[7] or magnetisation orientation[8].

In these devices, control over the orientation of the magnetisation comes about through magnetostriction[9]. Further advancements in artificial multiferroics have been achieved through the search for 1st-order magnetostrictive materials, such as in materials with large magnetovolume coupling. For example, switching between the low and high magnetisation states of the AFM and FM regimes in FeRh thin films shows a tenfold greater ME response with electric field dropped across the $BaTiO_3$ (BTO) substrate[10]. Here we investigate the Mn antiperovskite family of materials with giant magnetovolume coupling[11] and, importantly, magnetic frustration originating

from competing exchange interactions. As we show, it is the combination of these properties that allow for sensitive control of the magnetic state with applied strain through a direct process known as the piezomagnetic (PzM) effect[12], rather than through the commonly studied magnetostrictive effect.

In this report, we demonstrate the first experimental evidence of giant PzM in Mn-based antiperovskites using thin films of Mn_3NiN. PzM offers several clear advantages over magnetostriction; whilst magnetostriction underpinned by spin-orbit coupling is quadratic in strain (Figure 1a-b) and requires additional external magnetic fields for magnetisation reversal, PzM is a linear magneto-mechanic coupling that allows the magnetisation to be both controlled sensitively with small strains as well as its direction to be reversed by 180° (Figure 1c-d). These advantages make PzM an attractive and novel route to electric-field control of magnetism. Although theoretically predicted to occur in the Mn_3AN family, direct experimental verification

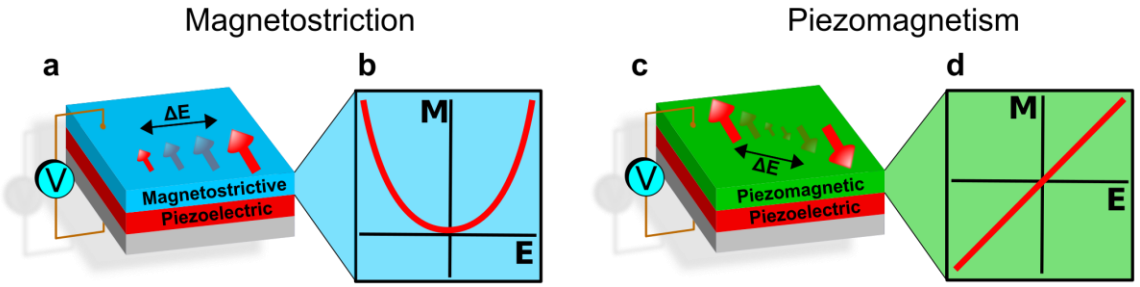

Figure 1. Current artificial multiferroic devices that control magnetisation with electric field rely on magnetostriction in multiferroic laminates as shown in (**a**). Magnetostriction varies quadratically with strain and is only significant in materials that possess large spin-orbit coupling. Device operation requires an external magnetic field to enable magnetisation reversal (**b**). In contrast, piezomagnetism (**c**) is linear in strain allowing sensitive control of magnetisation at small strains and, most importantly, magnetisation reversal without the need for an external magnetic field (**d**).

of its existance and magnitude remains an outstanding challenge.

Interesting properties of Mn_3AN bulk materials have been reported in the literature, for instance anomalous temperature dependence of resistivity[13], anomalous thermal expansion[14], giant barocaloric effects[15] and giant magnetovolume coupling[11]. As thin films, Mn_3NiN_{1-x}[16], Mn_3NiN[17,18] and a small number of other members of the Mn_3AN family (A = Cu and Ga)[19–23], have been grown. However, the focus has been primarily on growth and basic physical properties and previous experimental reports of piezomagnetism are absent.

First described in 1928[24] and studied in the 1960s[25], PzM was recognized to be a weak effect in some AFM materials such as CoF_2 and MnF_2, and in the intervening years predominantly ignored. An important development in the field was the recognition that the non-collinear AFM structure in the antiperovskite Mn_3GaN system lent itself sensitively to giant PzM effects. The effect was described phenomenologically in 1989[12], and the biaxial strain simulated by ab initio methods in 2008[26]. Most recently, ab initio theory predicted the PzM performance across a range of Mn-antiperovskites[27], finding large effects in other members of the family, whilst the strain phase diagram of Mn_3GaN has been extended to reveal a rich phase diagram of readily accessible magnetic states[28].

Figure 2(a) illustrates how the PzM effect is predicted to manifest in Mn_3NiN under biaxial strain. The magnetic structure shown is of the Γ^{4g} representation, in the notation of Fruchart *et al.*[29], which when unstrained, as shown by the red arrows, is a fully compensated AFM. Applying compressive or tensile biaxial strain, or indeed uniaxial strain, breaks the cubic symmetry of the lattice and the restriction that all moments are of equal magnitude. Moreover, the lattice strain causes an imbalance in the frustrated exchange interactions, leading to a continuous change in both the size and canting of the local Mn moments. The resulting net moment is induced in the [1/2,1/2,1] direction and can be reversed by 180° when switching from compressive to tensile strain. Thus, the PzM effect is a potentially powerful tool through which to control magnetisation.

Results and Discussion

In order to explore the PzM we study interface induced strain effects on single layer thin films of Mn_3NiN by growth on various substrates. Growth of a series of epitaxial thin films was achieved with thicknesses ranging from 20nm up to 100nm onto [001] oriented $SrTiO_3$ (STO), $(LaAlO_3)_{0.3}(Sr_2TaAlO_6)0.7$ (LSAT) and $BaTiO_3$ (BTO) single crystal substrates by means of nitrogen assisted pulsed laser deposition from a Mn_3NiN stoichiometric target (see Experimental Methods). Atomic resolution high-angle annular dark field scanning transmission electron microscopy (HAADF-STEM) and X-ray diffraction (XRD) analysis, examples of which are shown in Figures S1b,c, demonstrate the epitaxy of the thin films and compositional analysis (Table S1 and Figure S1a) confirm that beyond the first 3nm they are close to the expected 3:1:1 Mn:Ni:N stoichiometry. The STEM data reveal unusual growth of Mn_3NiN, whereby the films are lattice matched with the substrate at the interface, but far from the interface relax such that they are subjected to compressive (tensile) in-plane strain on substrates with larger (smaller) lattice parameters (Table S1). This abnormal relaxation is in agreement with the out-of-plane (OOP) XRD data of films grown on all substrates (Table S1). The in-plane lattice parameters of the films cannot be determined from grazing incidence XRD (as shown in supplementary Figure S2). Consequently, the Poisson's ratio of $\nu = 0.41$, which is calculated directly from the STEM data, and the OOP lattice parameter taken from the XRD data are used to provide the resulting in-plane biaxial strain for all films.

The temperature dependent magnetisation of the bulk material from which the target was made has a simple transition from a paramagnet to an AFM. In comparison, the films show a greatly broadened transition with a high temperature phase that has characteristics of a soft FIM as well as glass-like frustration (Figure S3). In the films, we define the transition to the AFM state, the Néel temperature (T_N), as the peak in the magnetisation versus temperature curve (Figure 2d and

S3a). Figure 2b shows that T_N varies systematically with the biaxial strain. The trend shows a linear dependence of T_N with a remarkable variation of approximately 60K with ±0.25% biaxial strain. The origin of the dependence of T_N on strain is the dissimilar scaling of the frustrated exchange interactions between the three Mn sites with strain. Moreover, as predicted the PzM induces a magnetisation in the films as shown in Figure 2c. The magnitudes of the induced moments are consistent with both our theoretical predictions and recent theoretical work on the related Mn antiperovskite system Mn_3GaN[28]. Although our films have a finite moment above

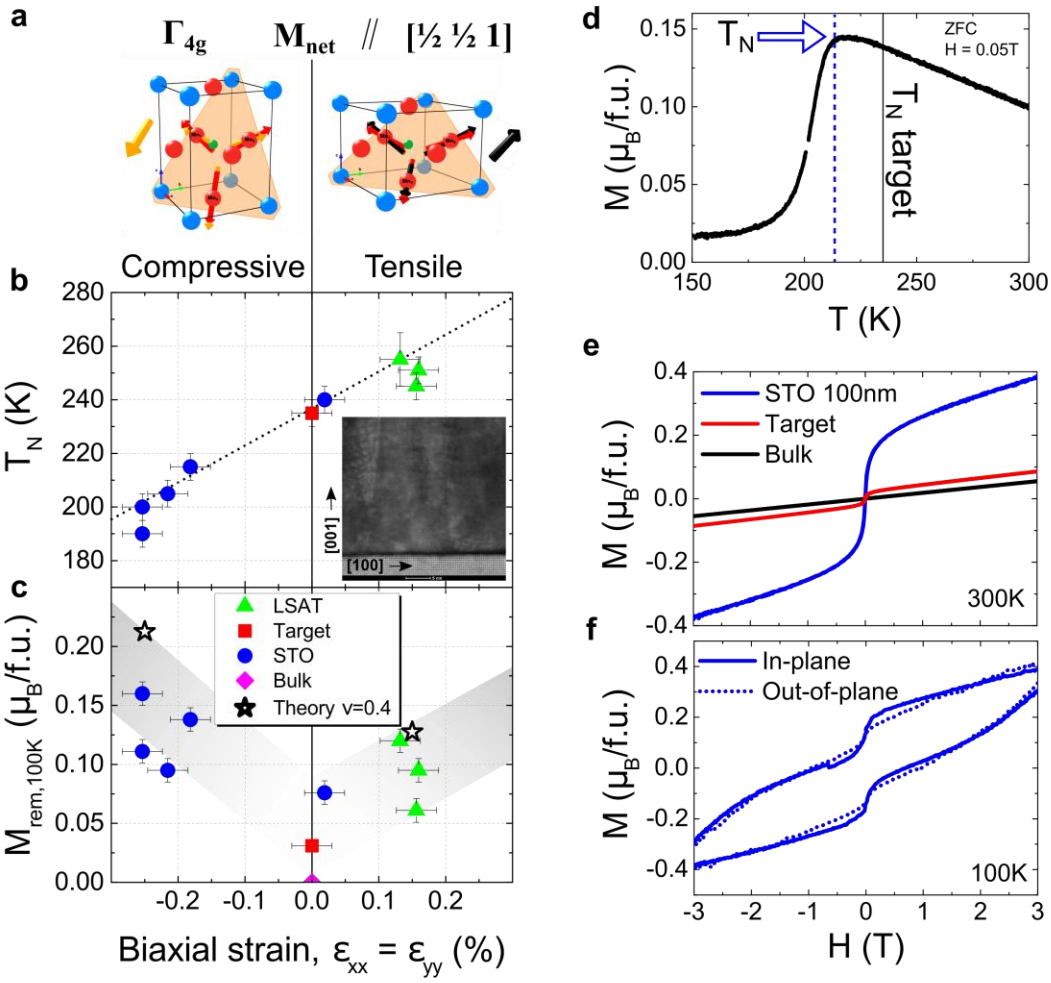

Figure 2. (**a**) Crystal and magnetic structure of Mn_3NiN. Red arrows in both panels indicate local magnetic moments on Mn sites according to Γ^{4g} representation in unstrained (cubic) lattice with $M_{net} = 0$. Yellow (black) arrows indicate magnetic moments under compressive (tensile) strain. M_{net} is parallel or antiparallel to M_{Mn3} with compressive and tensile strain, respectively. All magnetic moments are in the (111) plane indicated in orange. Canting and changes of size are not to scale; (**b**) Néel temperature as a function of biaxial strain, $\varepsilon_{xx} = \varepsilon_{yy}$, for all Mn_3NiN films (**inset**) HRTEM image of a Mn_3NiN film on STO; (**c**) Remnant magnetisation collected with field applied in plane for all samples. Bulk and target values are presented for comparison. Theory data is taken from [27] assuming a Poisson ratio ν=0.4, where $\varepsilon_{xx}/\varepsilon_{zz} = -2\nu/(1-\nu)$, in agreement with the value found with TEM; (**d**) Magnetisation as a function of temperature for a 100nm Mn_3NiN film grown on STO showing the shift of T_N; (**e**) $M(H)$ loop at 300K for the same film in (**d**) as well as the target and bulk samples; (**f**) $M(H)$ loop at 100K for the same film in (**d**) with the field applied in- or out-of-plane.

and below T_N this moment has quite different characteristics in these two regimes.

The $M(H)$ loops share a common property; above T_N the finite magnetisation state has the characteristics of a soft FIM state with zero hysteresis, whilst below T_N they have finite hysteresis and the loop opening survives to high magnetic field (Figure 2e and 2f). The latter is a characteristic feature of an AFM state where there is only weak coupling to the applied field. Figure 2f further demonstrates that the induced magnetisation has approximately equal components when the field is in-plane (IP) and out-of-plane (OOP), expected for the Γ^{4g} phase (cf. Figure 2a), and clearly inconsistent with the behaviour in the Γ^{5g} phase where the induced moment lies wholly in the (110) plane. In order to reverse the induced magnetisation by external magnetic field, the magnetocrystalline anisotropy has to be overcome and the moments must be rotated 180° in the (111) plane, the energy of which is determined solely by the spin-orbit coupling. We calculate a relatively weak anisotropy energy in Mn_3NiN ~ 0.1 meV/f.u. Converting this to a coercive field (H_c) using the induced moment observed at saturation extrapolated to M_s ~ 0.5 μ_B/f.u. gives H_c = 6.9T. Whilst this value is larger than that found experimentally by a factor of 2 approximately, the calculation corresponds to a simultaneous rotation of all Mn moments in the sample by 180°. The reduced H_c that we observe may be due to multi-domain effects[29]. This large coercivity in the AFM state, in contrast to the soft FIM state above T_N, underlies one of the elegant ways this material could be utilized in a non-volatile memory device.

To establish whether the induced magnetisation of Mn_3NiN in the AFM state can be changed by the application of in-situ strain, Mn_3NiN was grown on BTO [001] substrates. BTO has the advantage that it undergoes a number of structural transitions which distort its crystal structure and hence allow an in-situ change of strain; an effect utilised in a number of previous works[30–32] .

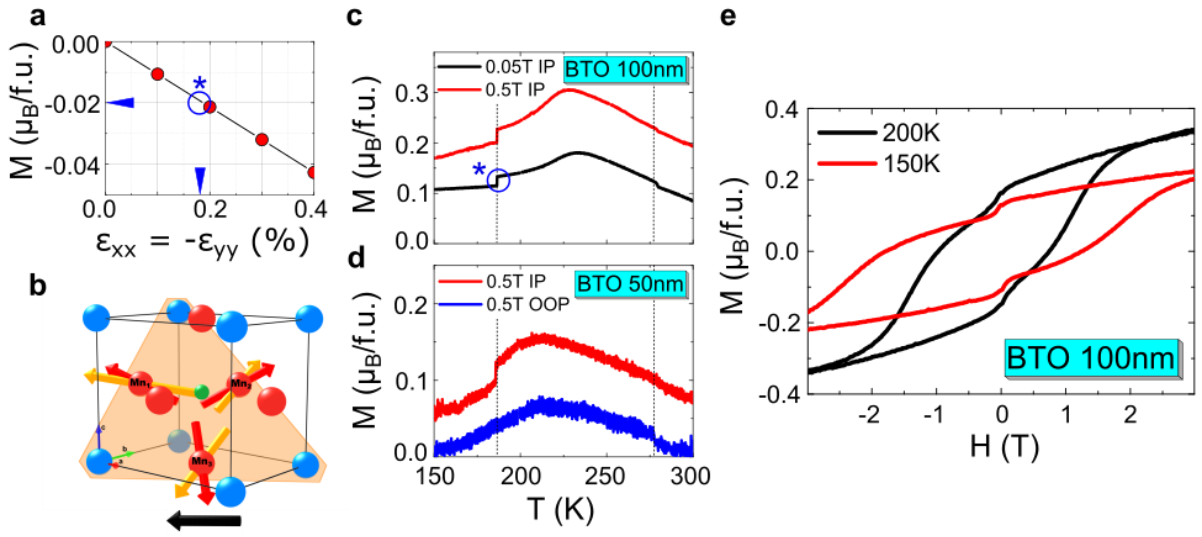

Figure 3. (**a**) Predicted variation in *M* with uniaxial strain. The blue circle, star symbol and horizontal arrow indicate the experimentally measured change in *M* from (**c**) and the vertical arrow indicates the inferred strain; (**b**) Predicted lattice and magnetic structure under uniaxial strain. The net moment (black) is wholly in the plane of the film; (**c-d**) Experimental *M*(*T*) of 100 and 50nm Mn_3NiN films on BTO showing a large jump in *M* at the orthorhombic to rhombohedral transition at 187K in BTO when measured with the applied field out-of-plane, which produces uniaxial strain; (**e**) the corresponding M(H) loops in the AFM state of Mn_3NiN above and below the 187K BTO transition.

Figure 3 summarises our findings for 100nm and 50nm thick Mn_3NiN films grown on BTO. At room temperature, the Mn_3NiN experiences compressive in-plane strain from growth on BTO. At the tetragonal to orthorhombic BTO structural transition at 275K the Mn_3NiN films are in the soft FIM state and we do not observe a strong change in the magnetisation. However, at the orthorhombic to rhombohedral BTO structural transition at 187K the films are in the AFM Γ^{4g} state and the magnetic properties are highly sensitive to strain. This structural transition of BTO is expected to induce a strain that is approximately uniaxial in the film[33]. Accordingly, we have calculated the magnitude of the induced net moment in response to this uniaxial strain, shown in Figure 3a, and predict that it lies wholly within the plane of the film (Figure 3b). Experimentally, both films on BTO show a large jump in magnetisation at the 187K BTO transition, shown in

Figures 3c and 3d, the magnitude of which is robust when the films are cooled in a large field of 0.5T. Crucially, the jump is only observed when the field is aligned in the plane of the film (Figure 3d), confirming our predictions of PzM behaviour resulting from uniaxial strain.

Further measurements of $M(H)$ loops above and below the 187K BTO transition for the 100nm film (Figure 3e) verify a uniform reduction in the saturation magnetisation and an increase in the field associated with flux closure. Moreover, using the calculated value of the resultant uniaxial strain, $\varepsilon_{xx} = -\varepsilon_{yy} = 0.45\%$[33], that the BTO substrate imposes, along with both the observed change of moment at the structural transition and our predictions shown in Figure 3a, we estimate that that the average strain experienced by the film is close to 0.2%, indicative of a 44% strain coupling efficiency. We estimate from these observations a magnetoelectric coefficient α, where $\alpha = \frac{dB}{dE}$, of 0.018 G cm/V (assuming 1% strain is achieved in BTO with 10 kV/cm[34]), in good agreement with the greater than 1000 fold increase over Cr_2O_3 ($\alpha = 2.67\text{x}10^{-6}$ G cm/V) predicted for this family of materials[26].

As PzM offers the opportunity for purely electric-field controlled magnetisation[27], implementation in devices of the giant PzM manifest in Mn antiperovskites requires compositions with T_N significantly above room temperature. Mn_3SnN has been predicted as an ideal composition with T_N of 475K and predicted piezomagnetic coefficient four times more sensitive than Mn_3NiN[27]. Alternatively, using a composition with T_N close to room temperature (such as Mn_3GaN with $T_N = 290$K[15]), by shifting the transition with strain the material can be isothermally switched between the hard AFM and soft FIM states. Both concepts open possibilities for novel non-volatile antiferromagnetic memory applications.

With giant PzM manifest in these materials, we foresee two unique device concepts where Mn_3AN could be utilised. The most direct write-procedure would be to identify a composition with T_N significantly above room temperature such that the magnetisation direction could be rotated in-

plane by 180°, using electric field induced biaxial strain, isothermally, in zero magnetic field and at room temperature. Mn_3SnN has been predicted as an ideal composition with T_N of 475K and predicted piezomagnetic coefficient four times more sensitive than Mn_3NiN[27]. An alternative concept would involve working with a composition with close to room temperature T_N (such as Mn_3GaN with T_N = 290K[15]). By controlling the T_N of such a system, again through electric field induced biaxial strain, the device could be cycled between the AFM and soft FIM state isothermally, allowing non-volatility (in the AFM state) and ease of writing (in the soft FIM state). Either concept opens up a fascinating future for novel non-volatile magnetic memory applications.

Conclusions

In summary, by scrutinising the systematic behaviour of films grown on different substrates we demonstrate experimentally that giant PzM is indeed manifest in antiferromagnetic Mn-based antiperovskites. Our Mn_3NiN thin films show significant changes of both Néel temperature and induced magnetisation due to the PzM effect, in excellent agreement with theory. These results pave the way to the development of piezoelectric multilayer heterostructures for direct electric-field control of strain and consequently, due to the nature of PzM, 180° rotation of magnetisation in the absence of applied magnetic field. Such a device offers significant novelty over current magnetostriction-based technologies. Additionally, as Mn_3SnN is predicted to deliver a fourfold increase in PzM compared to Mn_3NiN and has a T_N of 475K[27], advancing the development with this composition would be an important future work offering the prospect of room temperature PzM non-volatile memory devices.

Experimental Methods

High density PLD targets were prepared using a standard solid state synthesis technique along with spark plasma sintering (SPS). Firstly, $Mn_2N_{0.86}$ was formed by reacting elemental Mn powder (VWR, 325 mesh, 99.95 %) under dry, flowing nitrogen gas at 700°C for 48 hours. The refined lattice parameters of the $Mn_2N_{0.86}$ indicated this was the correct stoichiometry, rather than stoichiometric Mn_2N. Subsequently, the $Mn_2N_{0.86}$ precursor was ball-milled and then thoroughly mixed by hand with elemental Ni (Sigma Aldrich, < 150 μm, 99.99 %). The resulting mixture was pressed into several ~2g pellets, wrapped in Ta foil and sealed in evacuated quartz ampoules. The ampoules were heated to 780°C for 3 days before being quenched to room temperature in water. The pellets were again ball-milled, formed into a pellet and reacted at 780°C for 3 days to complete the reaction to the antiperovskite phase. The resulting pellets were ball-milled a final time before being sintered. The Mn_3NiN powder was placed in a high density graphite die with an inner diameter of 30 mm. In order to avoid any reaction between powder and graphite die and punches, a flexible graphite foil (0.45 mm thick) was lined internally in the graphite die and also on the active part of each punch. The die filled with the Mn_3NiN powder was then placed inside the SPS chamber. The parameters of the SPS experiment are as follow:

- sintering temperature: 800 °C;
- applied axial pressure during sintering: 35 MPa;
- holding time at sintering temperature (dwell): 10 min.;
- heating rate: 200 °C/min.;
- sintering atmosphere: Argon.

The temperature was measured by a K-type thermocouple placed in into a hole drilled in the graphite die (the distance between thermocouple and the sample was about 1 mm). After passing of the holding time at sintering temperature, the furnace was cooled down to room temperature

and the sample was ejected from the graphite die. The as obtained sample was cleaned in order to remove the graphite foil.

The Mn_3NiN thin films were deposited at 400ºC or 500 ºC by PLD using a KrF excimer laser (λ=248nm) with a laser fluency of 0.8 J/cm^2. In order to compensate the potential nitrogen loss during the growth, a flow of nitrogen was inserted into the chamber to keep the nitrogen partial pressure at 5 mTorr. After deposition, as grown films were slowly cooled down to room temperature at the growth partial pressure.

Crystalline structure analysis and phase determination of thin films were carried out by XRD (Philips X'Pert MRD system) with a CuKα radiation source. Out-of-plane lattice parameters were evaluated from conventional θ-2θ scans.

EDX presented in Table S1 were performed on an LEO Gemini 1525 FEGSEM. The FEGSEM is fitted with Oxford Instruments INCA energy dispersive and wavelength dispersive x-ray spectrometers. The spectra were acquired at a 10kV acceleration voltage and count contribution from both the films and substrate.

Atomic resolution HAADF-STEM images were taken on a probe corrected FEI Titan 3 80-300 S/TEM with a convergence angle of 24 mrad and annular detector range of approximately 70-480 mrad.

EDX and EELS were performed on an image corrected FEI Titan 3 G2 60-300 S/TEM with a quad-silicon drift SuperX EDX detection system and Gatan Quantum GIF. Hyperspectral EDX maps were recorded including the entire film thickness and some of the substrate, then line scans in the [001] direction were taken by horizontally averaging the hyperspectral maps to increase signal-to- noise and quantified using calculated Cliff-Lorimer k-factors. EELS line scans were also taken in the [001] direction with a convergence semiangle and collection angle of approximately 10 mrad and 60 mrad, respectively.

Magnetic measurements were performed using the VSM option in a Quantum Design Physical Property Measurement System (PPMS-9T). For in-plane measurements, films were mounted on quartz paddles secured using PTFE tape with the surface of the film parallel to the applied field. For out-of-plane measurements, films were secured in a plastic straw with the surface of the film perpendicular to the applied field. The magnetic contributions of the substrates were subtracted by measuring blank substrates using the same sample mounting techniques and measuring conditions. AC susceptibility was performed using the PPMS ACMS option.

All our calculations employ the projector augmented-wave (PAW) method[35] implemented in VASP code within the Perdew- Burke-Ernzerhof (PBE) generalized gradient approximation[36]. This approach allows for relaxation of fully unconstrained noncollinear magnetic structures[37]. We use a 12x12x12 k-point sampling in the self-consistent cycle and the cut-off energy is 400 eV. The local magnetic moments are evaluated in atomic spheres with the default Wigner-Seitz radius. The SO coupling is included but plays a negligible role in the PzM effect. We find the equilibrium lattice parameter and the Poisson's ratio for a system with fixed AFM order by fitting the total energies obtained for a range of lattice parameters (a, c/a) to Birch-Murnaghan equation of state as detailed in Ref. [27]. We obtain a = 0.384 nm and ν=0.15. Uniaxial strain is treated on the same footing as the biaxial strain. No symmetry of the unit cell is assumed as recommended for VASP simulation of any noncollinear magnetic structure.

ASSOCIATED CONTENT

The following files are available free of charge:

Supplementary figures (PDF)

AUTHOR INFORMATION

Corresponding Author

*David Boldrin, d.boldrin@imperial.ac.uk

Author Contributions

DB, APM, BZ, JZ and LFC conceived the experiments; DB and BVN made the targets and APM, BZ, PP grew films and provided structural characterisation; DB, LFC and LG provided magnetic characterisation; EW, BE and DWM provided TEM and associated characterisation; JZ performed the SDFT simulations, all authors contributed to the results, discussion and interpretation, and agree with the final version of the manuscript. ‡These authors contributed equally.

ACKNOWLEDGMENT

JZ, LFC and DB received funding from European Community 7th Framework Programme under grant agreement 310748 DRREAM and LFC and DB received funding from the UK EPSRC. We acknowledge support from the Henry Royce Institute made through EPSRC grant EP/R00661X/1 and EPSRC Impact Acceleration Account funding : Localised magnetic repository (LoMaRe) - a high performance non-volatile memory device.

SUPPORTING INFORMATION

Further characterisation of films, including: EDX profile from the TEM data, X-ray diffraction (XRD), magnetisation as a function of temperature, AC susceptibility. Collated structural information for all films from EDX, TEM and XRD data.

REFERENCES

1. Matsukura, F.; Tokura, Y.; Ohno, H. Control of magnetism by electric fields. *Nat. Nanotechnol.* **2015**, *10*, 209–220

2. Wang, J.; Neaton, J. B.; Zheng, H.; Nagarajan, V.; Ogale, S. B.; Liu, B.; Viehland, D.;

Vaithyanathan, V.; Schlom, D. G.; Waghmare, U. V; Spaldin, N. A.; Rabe, K. M.; Wuttig, M.; Ramesh, R. Epitaxial BiFeO$_3$ multiferroic thin film heterostructures. *Science (80-.).* **2003**, *299***,** 1719–1722

3. Eerenstein, W.; Mathur, N. D.; Scott, J. F.; F, J. Scott: Multiferroic and magnetoelectric materials. *Nature* **2006**, *442***,** 759–765

4. Chiba, D.; Fukami, S.; Shimamura, K.; Ishiwata, N.; Kobayashi, K.; Ono, T. Electrical control of the ferromagnetic phase transition in cobalt at room temperature. *Nat. Mater.* **2011**, *10***,** 853–856

5. Weiler, M.; Brandlmaier, A.; Geprägs, S.; Althammer, M.; Opel, M.; Bihler, C.; Huebl, H.; Brandt, M. S.; Gross, R.; Goennenwein, S. T. B. Voltage controlled inversion of magnetic anisotropy in a ferromagnetic thin film at room temperature. *New J. Phys.* **2009**, *11***,** 13021

6. Parkes, D. E.; Cavill, S. A.; Hindmarch, A. T.; Wadley, P.; McGee, F.; Staddon, C. R.; Edmonds, K. W.; Campion, R. P.; Gallagher, B. L.; Rushforth, A. W. Non-volatile voltage control of magnetization and magnetic domain walls in magnetostrictive epitaxial thin films. *Appl. Phys. Lett.* **2012**, *101***,** 72402

7. Molegraaf, H. J. A.; Hoffman, J.; Vaz, C. A. F.; Gariglio, S.; Van Der Morel, D.; Ahn, C. H.; Triscone, J. M. Magnetoelectric effects in complex oxides with competing ground states. *Adv. Mater.* **2009**, *21***,** 1–5

8. Heron, J. T.; Trassin, M.; Ashraf, K.; Gajek, M.; He, Q.; Yang, S. Y.; Nikonov, D. E.; Chu, Y. H.; Salahuddin, S.; Ramesh, R. Electric-field-induced magnetization reversal in a ferromagnet-multiferroic heterostructure. *Phys. Rev. Lett.* **2011**, *107***,** 1–5

9. Ramesh, R.; Spaldin, N. A. Multiferroics: progress and prospects in thin fi lms. *Nat. Mater.*

2007, *6*, 21–29

10. Cherifi, R. O.; Ivanovskaya, V.; Phillips, L. C.; Zobelli, A.; Infante, I. C.; Jacquet, E.; Garcia, V.; Fusil, S.; Briddon, P. R.; Guiblin, N.; Mougin, A.; Ünal, a a; Kronast, F.; Valencia, S.; Dkhil, B.; Barthélémy, A.; Bibes, M. Electric-field control of magnetic order above room temperature. *Nat. Mater.* **2014**, *13*, 345–51

11. Takenaka, K.; Ichigo, M.; Hamada, T.; Ozawa, A.; Shibayama, T.; Inagaki, T.; Asano, K. Magnetovolume effects in manganese nitrides with antiperovskite structure. *Sci. Technol. Adv. Mater.* **2014**, *15*, 15009–11

12. Gomonaj, E. V. Magnetostriction and piezomagnetism of noncollinear antiferromagnet Mn3NiN. *Phase Transitions* **1989**, *18*, 93–101

13. Chi, E. O.; Kim, W. S.; Hur, N. H. Nearly zero temperature coefficient of resistivity in antiperovskite compound CuNMn3. *Solid State Commun.* **2001**, *120*, 307–310

14. Deng, S.; Sun, Y.; Wu, H.; Huang, Q.; Yan, J.; Shi, K.; Malik, M. I.; Lu, H.; Wang, L.; Huang, R.; Li, L.; Wang, C. Invar-like Behavior of Antiperovskite Mn 3+x Ni 1−x N Compounds. *Chem. Mater.* **2015**, *27*, 2495–2501

15. Matsunami, D.; Fujita, A.; Takenaka, K.; Kano, M. Giant barocaloric efect enhanced by the frustration of the antiferromagnetic phase in Mn 3 GaN. *Nat. Mater.* **2014**, *14*, 73–78

16. Na, Y.; Wang, C.; Xiang, J. Structural and magnetic properties of antiperovskite Mn 3 NiN x thin films. *Mater. Lett.* **2015**, *152*, 213–216

17. Na, Y.; Wang, C.; Chu, L.; Ding, L.; Yan, J.; Xue, Y.; Xie, W.; Chen, X. Preparation and properties of antiperovskite Mn3NiN thin film. *Mater. Lett.* **2011**, *65*, 3447–3449

18. Na, Y.; Wang, C.; Tomasella, E.; Cellier, J.; Xiang, J. Effect of Cu doping on structural and magnetic properties of antiperovskite Mn3Ni(Cu)N thin films. *J. Alloys Compd.* **2015**, *647*, 35–40

19. Shi, K.; Wang, C.; Sun, Y.; Wang, L.; Deng, S.; Hu, P.; Lu, H.; Hao, W.; Wang, T.; Tang, W. Rectifying Characteristics and Semiconductor-Metal Transition Induced by Interfacial Potential in the Mn3CuN/n-Si Intermetallic Heterojunction. *ACS Appl. Mater. Interfaces* **2017**, *9*, 12592–12600

20. Sakakibara, H.; Ando, H.; Kuroki, Y.; Kawai, S.; Ueda, K.; Asano, H. Magnetic properties and anisotropic magnetoresistance of antiperovskite nitride Mn_3GaN/Co_3FeN exchange-coupled bilayers. *J. Appl. Phys.* **2015**, *117*, 17D725

21. Lee, H.; Sukegawa, H.; Liu, J.; Ohkubo, T.; Kasai, S.; Mitani, S.; Hono, K. Ferromagnetic MnGaN thin films with perpendicular magnetic anisotropy for spintronics applications. *Appl. Phys. Lett.* **2015**, *107*, 1–6

22. Aoyama, M.; Takenaka, K.; Ikuta, H. Sputter deposition and characterization of Mn3CuN thin films. *J. Alloys Compd.* **2013**, *577*, S314–S317

23. Sun, Y.; Wang, C.; Na, Y.; Chu, L.; Wen, Y.; Nie, M. Investigation of antiperovskite Mn3CuNx film prepared by DC reactive magnetron sputtering. *Mater. Res. Bull.* **2010**, *45*, 1230–1233

24. Voigt, W. *Lehrbuch der Kristallphysik*. (B.G. Teubner, **1928**).

25. Borovnik-Romanov, A. S. Piezomagnetism in the Antiferromagnetic Fluorides of Cobalt and Manganese. *Sov. Phys. JETP* **1960**, *11*, 786–793

26. Lukashev, P.; Sabirianov, R. F.; Belashchenko, K. Theory of the piezomagnetic effect in Mn-based antiperovskites. *Phys. Rev. B* **2008**, *78*, 184414

27. Zemen, J.; Gercsi, Z.; Sandeman, K. G. Piezomagnetic effect as a counterpart of negative thermal expansion in magnetically frustrated Mn-based antiperovskite nitrides. *Phys. Rev. B* **2017**, *96*, 24451

28. Zemen, J.; Mendive-Tapia, E.; Gercsi, Z.; Banerjee, R.; Staunton, J. B.; Sandeman, K. G. Frustrated magnetism and caloric effects in Mn-based antiperovskite nitrides: Ab initio theory. *Phys. Rev. B* **2017**, *95*, 184438

29. Fruchart, D.; Bertaut, E. F. Magnetic Studies of the Metallic Perovskite-Type Compounds of Manganese. *J. Phys. Soc. Japan* **1978**, *44*, 781

30. Phillips, L. C.; Cherifi, R. O.; Ivanovskaya, V.; Zobelli, A.; Infante, I. C.; Jacquet, E.; Guiblin, N.; Ünal, a. a.; Kronast, F.; Dkhil, B.; Barthélémy, A.; Bibes, M.; Valencia, S. Local electrical control of magnetic order and orientation by ferroelastic domain arrangements just above room temperature. *Sci. Rep.* **2015**, *5*, 10026

31. Thiele, J. U.; Maat, S.; Fullerton, E. E. FeRH/FePt exchange spring films for thermally assisted magnetic recording media. *Appl. Phys. Lett.* **2003**, *82*, 2859–2861

32. Bennett, S. P.; Wong, A. T.; Glavic, A.; Herklotz, A.; Urban, C.; Valmianski, I.; Biegalski, M. D.; Christen, H. M.; Ward, T. Z.; Lauter, V. Giant Controllable Magnetization Changes Induced by Structural Phase Transitions in a Metamagnetic Artificial Multiferroic. *Sci. Rep.* **2016**, *6*, 1–7

33. Aroyo, M. I.; Perez-Mato, J. M.; Capillas, C.; Kroumova, E.; Ivantchev, S.; Madariaga, G.; Kirov, A.; Wondratschek, H. Bilbao Crystallographic Server: I. Databases and

crystallographic computing programs. *Zeitschrift fur Krist.* **2006**, *221***,** 15–27

34. Rafique, M.; Herklotz, A.; Dörr, K.; Manzoor, S. Giant room temperature magnetoelectric response in strain controlled nanocomposites. *Appl. Phys. Lett.* **2017**, *110***,** 0–5

35. Kresse, G. From ultrasoft pseudopotentials to the projector augmented-wave method. *Phys. Rev. B* **1999**, *59***,** 1758–1775

36. Perdew, J. P.; Burke, K.; Ernzerhof, M. Generalized Gradient Approximation Made Simple. *Phys. Rev. Lett.* **1996**, *77***,** 3865–3868

37. Hobbs, D.; Kresse, G.; Hafner, J. Fully unconstrained noncollinear magnetism within the projector augmented-wave method. *Phys. Rev. B - Condens. Matter Mater. Phys.* **2000**, *62***,** 11556–11570

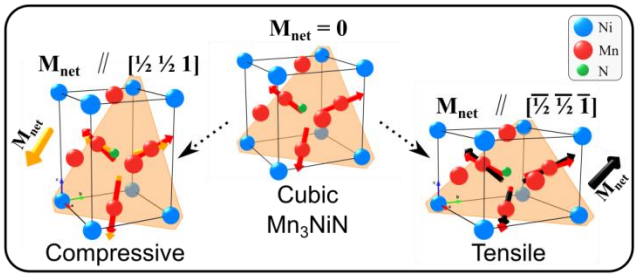
M_{net} = 0
M_{net} // [½ ½ 1]
M_{net} // [$\bar{1}$/2 $\bar{1}$/2 $\bar{1}$]
Ni
Mn
N
Cubic
Mn_3NiN
Compressive
Tensile

TOC Figure